

Optimized production of ultracold ground-state molecules: Stabilization employing potentials with ion-pair character and strong spin-orbit coupling

Michał Tomza,^{1,2} Michael H. Goerz,² Monika Musiał,³ Robert Moszynski,¹ and Christiane P. Koch^{2,*}

¹*Faculty of Chemistry, University of Warsaw, Pasteura 1, 02-093 Warsaw, Poland*

²*Theoretische Physik, Universität Kassel, Heinrich-Plett-Str. 40, 34132 Kassel, Germany*

³*Institute of Chemistry, University of Silesia, Szkolna 9, 40-006 Katowice, Poland*

(Received 10 August 2012; published 22 October 2012)

We discuss the production of ultracold molecules in their electronic ground state by photoassociation employing electronically excited states with ion-pair character and strong spin-orbit interaction. A short photoassociation laser pulse drives a nonresonant three-photon transition for alkali-metal atoms colliding in their lowest triplet state. The excited-state wave packet is transferred to the ground electronic state by a second laser pulse, driving a resonant two-photon transition. After analyzing the transition matrix elements governing the stabilization step, we discuss the efficiency of population transfer using transform-limited and linearly chirped laser pulses. Finally, we employ optimal control theory to determine the most efficient stabilization pathways. We find that the stabilization efficiency can be increased by one and two orders of magnitude when using linearly chirped and optimally shaped laser pulses, respectively.

DOI: [10.1103/PhysRevA.86.043424](https://doi.org/10.1103/PhysRevA.86.043424)

PACS number(s): 33.80.-b, 82.53.Kp, 31.50.-x, 33.90.+h

I. INTRODUCTION

Photoassociation, which is the forming of molecules from ultracold atoms using laser light [1], is a prime candidate for coherent control which utilizes the wave nature of matter in order to steer a process, such as the formation of a chemical bond, toward a desired target [2,3]. At very low temperature, the delicate buildup of constructive and destructive interference between different quantum pathways is not hampered by thermal averaging. The basic tool for coherent control are short laser pulses that can be shaped in their amplitude, phase, and polarization. They can drive both adiabatic and nonadiabatic photoassociation dynamics [4].

A particular feature of photoassociation at very low temperatures is the excitation of an atom pair at fairly large interatomic separations [1]. This results from a compromise between the atom pair density in the electronic ground state, highest at large interatomic separations, and the population of excited-state bound levels with reasonable binding energies, which increase with decreasing interatomic separations. Therefore, the free-to-bound transition matrix elements are largest for photoassociation at separations of $50a_0$ to $150a_0$ with corresponding detunings of less than about 20 cm^{-1} . Although these matrix elements are optimally chosen, they are several orders of magnitude smaller than those for the excitation of atoms. This poses a problem for photoassociation with short laser pulses which inherently have a large bandwidth. As soon as the wings of the pulse spectrum overlap with the atomic resonance, atoms instead of bound levels are excited [5], and subsequent spontaneous emission depletes the trapped sample [6,7]. In photoassociation experiments using broadband femtosecond laser pulses, the pulse spectrum therefore needed to be cut to suppress excitation of the atomic resonance [8]. The sharp spectral cut yields long wings of the temporal pulse profile, and the ensuing photoassociation dynamics were dominated by transient Rabi oscillations of extremely weakly bound molecules caused by the long tail

of the pulse [8–11]. While it was gratifying to see that femtosecond photoassociation is feasible [8], larger binding energies and vibrational instead of electronic dynamics are required to produce stable molecules in their electronic ground state [4].

Femtosecond photoassociation at very low temperature corresponds to driving a narrow-band transition with a broadband laser. This can be achieved by employing multiphoton rather than one-photon transitions [12]. The high peak powers of femtosecond laser pulses easily allow for driving multiphoton transitions, and multiphoton control schemes have been demonstrated for both weak [12,13] and strong laser pulses [14–16]. In the weak-field regime, perturbation theory shows that optical interference of two or more photons can be used to completely suppress absorption [12,13]. For intermediate intensities, higher-order perturbation theory can be employed to obtain rational pulse shapes that allow the absorption to be controlled [17–21]. In the strong-field regime, dynamic Stark shifts drive the transition out of resonance. This can be countered by a linear chirp of the pulse which compensates the phase accumulated due to the Stark shift. Additionally, adjusting the amplitude of the pulse to guarantee a π or 2π pulse controls the absorption [14–16]. These control schemes can be applied to femtosecond photoassociation in order to suppress the excitation of atoms [22]. Multiphoton transitions can also be useful for femtosecond photoassociation at high temperature [23,24]. There the main advantage derives from the larger flexibility in transition energies, obtained when combining two or more photons, and the new selection rules. The disadvantage of high temperatures is the low initial coherence, or quantum purity, of the thermal ensemble of atoms. However, femtosecond photoassociation can generate rovibrational coherence by Franck-Condon filtering [23]. The long-standing goal of coherently controlling bond formation [25] has thus become within reach also for high temperatures.

Besides the possibility of driving a narrow-band transition, multiphoton femtosecond photoassociation also allows for accessing highly excited electronic states that may have significant ion-pair character. Such states are expected to

*christiane.koch@uni-kassel.de

the Hamiltonian describing the three-photon photoassociation reads

$$\hat{H}_{\text{pump}}(t) = \begin{pmatrix} \hat{H}^{a^3\Sigma_u^+}(R) & 0 & \epsilon^*(t)^3\chi^{(3)}(\omega_L, R) & 0 \\ 0 & \hat{H}^{(5)^1\Sigma_g^+}(R) & \xi_3(R) & A(R) \\ \epsilon(t)^3\chi^{(3)}(R) & \xi_3(R) & \hat{H}^{(3)^3\Pi_g}(R) - \xi_4(R) & \xi_5(R) \\ 0 & A(R) & \xi_5(R) & \hat{H}^{(6)^1\Sigma_g^+}(R) \end{pmatrix} \quad (1)$$

in the (three-photon) rotating-wave approximation. In Eq. (1), $\hat{H}^{2S+1|\Lambda|}$ denotes the Hamiltonian for the nuclear motion in the $^{2S+1}|\Lambda|$ electronic state,

$$\hat{H}^{2S+1|\Lambda|} = \hat{T} + V^{2S+1|\Lambda|}(R) + \omega_S^{2S+1|\Lambda|}(t, R) + \Delta_{\omega_L}, \quad (2)$$

where the kinetic energy operator is given by $\hat{T} = \frac{\hbar^2}{2\mu} \frac{d^2}{dR^2}$, μ is the reduced mass, and $V^{2S+1|\Lambda|}(R)$ is the potential-energy curve. The three-photon detuning, Δ_{ω_L} is taken with respect to the atomic $^2S(5s) \rightarrow ^2P_{1/2}(6p)$ three-photon transition. For strong photoassociation laser pulses, the dynamic Stark shift, $\omega_S^{2S+1|\Lambda|}(t, R)$, will become significant. It arises from the interaction of the $^{2S+1}|\Lambda|$ state with the intermediate off-resonant states and is given by the effective dynamic electric dipole polarizability, $\alpha_{\text{eff}}(\omega_L, R)$,

$$\omega_S^{2S+1|\Lambda|}(t, R) = -\frac{1}{2}|\epsilon(t)|^2\alpha_{\text{eff}}(\omega_L, R), \quad (3)$$

where $\epsilon(t) = |\epsilon(t)|e^{i\phi(t)}$ describes the electric field of the laser pulse in the rotating frame with envelope $|\epsilon(t)|$ and $\phi(t)$ denoting the relative phase, taken with respect to the central frequency's phase. $\chi^{(3)}(\omega_L, R)$ is the three-photon electric dipole transition moment, $\xi_i(R)$ ($i = 3, 5$) are the spin-orbit couplings, and $A(R)$ is the nonadiabatic radial coupling matrix element between the $(5)^1\Sigma_g^+$ and $(6)^1\Sigma_g^+$ states.

In a second step, the initial wave packet created by the three-photon photoassociation is deexcited to the $X^1\Sigma_g^+$ ground electronic state via a resonant two-photon electric dipole transition. The intermediate states for the two-photon transition are the $A^1\Sigma_u^+$ and $b^3\Pi_u$ states, correlating to the $^2S(5s) + ^2P(5p)$ asymptote and which are also strongly coupled by the spin-orbit interaction. Electric dipole transitions are allowed between all components of the initial wave packet and the intermediate states, whereas the $X^1\Sigma_g^+$ ground electronic state is only connected to the $A^1\Sigma_u^+$ state by a strong electric dipole transition. The Hamiltonian describing the stabilization of the photoassociated wave packet to the electronic ground state via a resonant two-photon transition reads

$$\hat{H}_{\text{dump}}(t) = \begin{pmatrix} \hat{H}^{X^1\Sigma_g^+}(R) & \epsilon^*(t)d_1(R) & 0 & 0 & 0 & 0 \\ \epsilon(t)d_1(R) & \hat{H}^{A^1\Sigma_u^+}(R) & \xi_1(R) & \epsilon^*(t)d_2(R) & 0 & \epsilon^*(t)d_4(R) \\ 0 & \xi_1(R) & \hat{H}^{b^3\Pi_u}(R) - \xi_2(R) & 0 & \epsilon^*(t)d_3(R) & 0 \\ 0 & \epsilon(t)d_2(R) & 0 & \hat{H}^{(5)^1\Sigma_g^+}(R) & \xi_3(R) & A(R) \\ 0 & 0 & \epsilon(t)d_3(R) & \xi_3(R) & \hat{H}^{(3)^3\Pi_g}(R) - \xi_4(R) & \xi_5(R) \\ 0 & \epsilon(t)d_4(R) & 0 & A(R) & \xi_5(R) & \hat{H}^{(6)^1\Sigma_g^+}(R) \end{pmatrix}, \quad (4)$$

in a (one-photon) rotating-wave approximation. The Hamiltonian for field-free nuclear motion in the $^{2S+1}|\Lambda|$ electronic state, $\hat{H}^{2S+1|\Lambda|}$, is now given by

$$\hat{H}^{2S+1|\Lambda|} = \hat{T} + V^{2S+1|\Lambda|}(R) + \Delta_{\omega_L}^{np}, \quad (5)$$

with the detunings $\Delta_{\omega_L}^{5p} = \omega_{2P(5p)} - \omega_L$ and $\Delta_{\omega_L}^{6p} = \omega_{2P(6p)} - 2\omega_L$ for the states dissociating into the $^2S(5s) + ^2P(5p)$ and $^2S(5s) + ^2P(6p)$ asymptotes, respectively. The electric transition dipole moments are denoted by

$$\begin{aligned} d_1(R) &= \langle X^1\Sigma_g^+ | \hat{d} | A^1\Sigma_u^+ \rangle, & d_2(R) &= \langle A^1\Sigma_u^+ | \hat{d} | (5)^1\Sigma_g^+ \rangle, \\ d_3(R) &= \langle b^3\Pi_u | \hat{d} | (3)^3\Pi_g \rangle, & d_4(R) &= \langle A^1\Sigma_u^+ | \hat{d} | (6)^1\Sigma_g^+ \rangle, \end{aligned}$$

and the spin-orbit coupling matrix elements read

$$\begin{aligned} \xi_1(R) &= \langle A^1\Sigma_u^+ | \hat{H}_{\text{SO}}^{\Omega=0_u^+} | b^3\Pi_u \rangle, \\ \xi_2(R) &= \langle b^3\Pi_u | \hat{H}_{\text{SO}}^{\Omega=0_u^+} | b^3\Pi_u \rangle, \\ \xi_3(R) &= \langle (5)^1\Sigma_g^+ | \hat{H}_{\text{SO}}^{\Omega=0_g^+} | (3)^3\Pi_g \rangle, \\ \xi_4(R) &= \langle (3)^3\Pi_g | \hat{H}_{\text{SO}}^{\Omega=0_g^+} | (3)^3\Pi_g \rangle, \\ \xi_5(R) &= \langle (6)^1\Sigma_g^+ | \hat{H}_{\text{SO}}^{\Omega=0_g^+} | (3)^3\Pi_g \rangle, \end{aligned}$$

where \hat{H}_{SO} denotes the spin-orbit Hamiltonian in the Breit-Pauli approximation. For large interatomic separations R , the transition dipole moments and spin-orbit coupling approach,

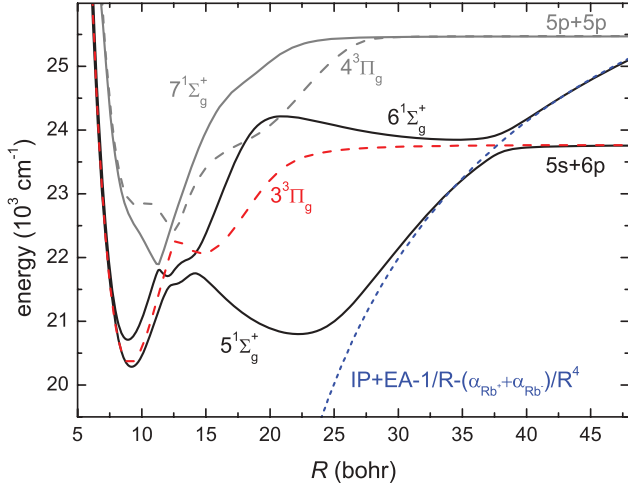


FIG. 2. (Color online) The $(5) 1\Sigma_g^+$, $(6) 1\Sigma_g^+$, and $(3) 3\Pi_g$ electronic states relevant for initial wave packet dynamics and ion-pair curve.

shown in Fig. 3, their atomic values,

$$\begin{aligned} d_1(R \rightarrow \infty) &= \sqrt{2} \langle 2S(5s) | \hat{d} | 2P(5p) \rangle, \\ d_2(R \rightarrow \infty) &= 0, \quad d_3(R \rightarrow \infty) = 0, \\ d_4(R \rightarrow \infty) &= \sqrt{2} \langle 2S(5s) | \hat{d} | 2P(5p) \rangle, \end{aligned}$$

and

$$\begin{aligned} \xi_2(R \rightarrow \infty) &= \xi_1(R \rightarrow \infty) / \sqrt{2} = \Delta_{FS}(2P(6p)) / 3, \\ \xi_4(R \rightarrow \infty) &= \xi_3(R \rightarrow \infty) / \sqrt{2} = \Delta_{FS}(2P(5p)) / 3, \\ \xi_5(R \rightarrow \infty) &= 0, \end{aligned}$$

where $\Delta_{FS}(2P(5p)) = 237.6 \text{ cm}^{-1}$ and $\Delta_{FS}(2P(6p)) = 77.5 \text{ cm}^{-1}$ are the atomic fine structure splittings.

The Hamiltonians (1) and (4) are represented on a Fourier grid with an adaptive step size [37–39] using $N = 2048$ grid points. The time-dependent Schrödinger equation for the pump

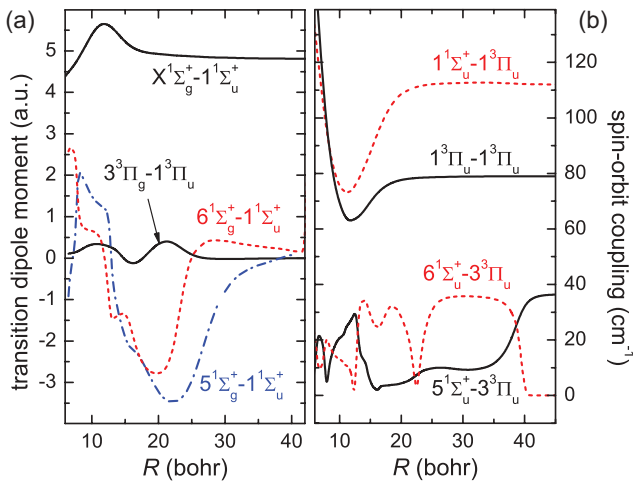


FIG. 3. (Color online) Electric transition dipole moments (a) and spin-orbit coupling matrix elements (b) essential for the dynamics studied.

and dump Hamiltonians,

$$i \frac{\partial}{\partial t} |\Psi(t)\rangle = \hat{H} |\Psi(t)\rangle, \quad (6)$$

is solved by the Chebyshev propagator [40].

B. Electronic structure

State-of-the-art *ab initio* techniques have been applied to determine the electronic structure data of the rubidium molecule needed in our dynamical models of the pump and dump processes. The details of the calculations and a thorough discussion of the accuracy by comparison with the most recent high-resolution spectroscopic results will be reported elsewhere [41]. Briefly, all potential-energy curves for the gerade and ungerade singlet and triplet states lying below 26000 cm^{-1} at the dissociation limit were calculated with the recently introduced double electron attachment intermediate Hamiltonian Fock space coupled cluster method restricted to single and double excitations (DEA-IH-FS-CCSD) [42,43]. Starting with the closed-shell reference state for the doubly ionized molecule Rb_2^{2+} that shows the correct dissociation at large distances R into closed-shell subsystems, $\text{Rb}^+ + \text{Rb}^+$, and using the double electron attachment operators in the Fock space coupled cluster ansatz renders our method size-consistent at any interatomic distance R and guarantees the correct large- R asymptotics. Thus, the DEA-IH-FS-CCSD approach overcomes the problem of the standard CCSD and equation of motion CCSD methods [44] with the proper dissociation into open-shell atoms. The potential-energy curves obtained from the *ab initio* calculations were smoothly connected at intermediate distances to the asymptotic multipole expansion [45]. The C_6 coefficient of the electronic ground state and the C_3 coefficient of the first excited state were fixed at their empirical values derived from high-resolution spectroscopic experiments [46,47], while the remaining coefficients were taken from Ref. [48]. Electric transition dipole moments, radial nonadiabatic coupling, and spin-orbit-coupling matrix elements were obtained by the multireference configuration interaction method (MRCI), restricted to single and double excitations with a large active space. Scalar relativistic effects were included by using the small-core fully relativistic energy-consistent pseudopotential ECP28MDF [49] from the Stuttgart library. Thus, in the present study the Rb_2 molecule was treated as a system of effectively 18 electrons. This basis was obtained by decontracting and augmenting the basis set of Ref. [49] by a set of additional functions, improving the accuracy of the atomic excitation energies of the rubidium atom with respect to the NIST database. With this basis set, employing the DEA-IH-FS-CCSD method for the nonrelativistic energies and the MRCI approach for the fine structure, we reproduce the experimental excitation energies with a root mean square deviation (rmsD) of 21 cm^{-1} . The DEA-IH-FS-CCSD calculations were done with the code based on the ACES II program system [50], while the MRCI calculations were performed with the MOLPRO code [51].

The accuracy of the computed potential-energy curves is as excellent as that of the atomic excitation energies [41]. Here, we only point out that the rmsD of the well depths of the present

potential-energy curves for electronic states that were observed experimentally is 64 cm^{-1} . In particular, the well depths of the ground singlet state and the lowest triplet state are reproduced within 2.7% and 3.7%, respectively. The relative errors for the excited states relevant for the present study, the $A^1\Sigma_u^+$ and $b^3\Pi_u$ pair, are even smaller at 0.5% and 0.3%, respectively. We expect a similar accuracy for the higher electronic states that have not yet been observed experimentally. The accuracy of the present results for the potential-energy curves is much higher than that of Refs. [52,53] and slightly better than in the recent study by Allouche and Aubert-Frécon [54], which did not consider the electronic states crucial for our photoassociation proposal.

C. Optimal control theory

Optimal control theory (OCT) can be used to calculate the shape of laser pulses that efficiently drive a desired transition. We will employ it here to determine the most efficient stabilization between an initial molecular wave packet and deeply bound levels in the ground electronic state. In principle, this problem is completely controllable such that perfect population transfer can be realized. However, constraints such as limited pulse duration, spectral bandwidth, and pulse intensity will compromise the stabilization process, reducing the transfer efficiency.

The control problem is defined by minimization of the functional

$$J = J_T + \int_0^T g[\epsilon(t)]dt, \quad (7)$$

where the first term denotes the final-time T target and the second one denotes the intermediate-time costs. The final-time target J_T can be chosen to correspond to a single state-to-state transition J_T^{ss} or to the transition into a manifold of final states, J_T^{sm} . For a single state-to-state transition from an initial state $|\Psi_{\text{in}}\rangle$ to a target state, here a vibrational level of the electronic ground state, v'' , the final-time functional is written as

$$J_T^{ss} = 1 - |\langle \Psi_{v''} | \hat{U}(T, 0; \epsilon) | \Psi_{\text{in}} \rangle|^2. \quad (8)$$

$\hat{U}(T, 0; \epsilon) | \Psi_{\text{in}} \rangle$ represents the formal solution of the time-dependent Schrödinger equation with $\hat{U}(T, 0; \epsilon)$ being the time evolution operator. J_T^{ss} corresponds to the overlap of the initial state, propagated to the final time T under the action of the laser field $\epsilon(t)$, with the target state. Optimizing a transition into a manifold of states is expressed by the functional

$$J_T^{sm} = 1 - \sum_{v''=v''_{\min}}^{v''_{\max}} |\langle \Psi_{v''} | \hat{U}(T, 0; \epsilon) | \Psi_{\text{in}} \rangle|^2, \quad (9)$$

where any vibrational level of the electronic ground state with quantum number between v''_{\min} and v''_{\max} can be populated at the final time. Once the optimum is reached, both functionals J_T^{ss} and J_T^{sm} take the value zero.

The intermediate-time cost, $g[\epsilon(t)]$ can in general depend on both the state and the field. Here, we restrict the dependence to one on the laser field only, where we ask that optimization does not change or changes only minimally the integrated

pulse energy

$$g[\epsilon(t)] = \frac{\lambda}{S(t)} \sum_{a=\{\text{Re}, \text{Im}\}} (\epsilon_a^{(k+1)}(t) - \epsilon_a^{(k)}(t))^2, \quad (10)$$

with k labeling the iteration step [55]. The shape function $S(t)$, $S(t) = \sin^2(\pi t/T)$, enforces a smooth switch on and off of the field and λ is a weight. Note that the laser field is complex since we employ the rotating-wave approximation. A nonzero phase indicates a relative phase with respect to the laser-pulse peak center or, in the spectral domain, with respect to the phase of the central laser frequency.

Using the linear variant of Krotov's method [56,57], the update equation for the laser field at iteration step $k+1$ can be derived:

$$\begin{aligned} & \text{Re}[\epsilon^{(k+1)}(t)] \\ &= \text{Re}[\epsilon^{(k)}(t)] - \frac{S(t)}{2\lambda} \text{Im} \left[\sum_{v''=v''_{\min}}^{v''_{\max}} \langle \Psi_{\text{in}} | \hat{U}^\dagger(T, 0; \epsilon^{(k)}) | \Psi_{v''} \rangle \right. \\ & \quad \left. \times \langle \Psi_{v''} | \hat{U}^\dagger(t, T; \epsilon^{(k)}) \frac{\partial \hat{H}_{\text{dump}}}{\partial \text{Re}[\epsilon]} \Big|_{\epsilon^{(k+1)}} \hat{U}(t, 0; \epsilon^{(k+1)}) | \Psi_{\text{in}} \rangle \right], \end{aligned} \quad (11)$$

and analogously for $\text{Im}[\epsilon^{(k+1)}(t)]$, where $\hat{U}(t, 0; \epsilon^{(k+1)}) | \Psi_{\text{in}} \rangle$ is the initial state forward propagated to time t under the action of the new field, $\epsilon^{(k+1)}$, and $\hat{U}(t, T; \epsilon^{(k)}) | \Psi_{v''} \rangle$ denotes the target state(s) backward propagated to time t under the action of the old field, $\epsilon^{(k)}$. The derivative of the Hamiltonian with respect to the field yields a matrix having as its elements all the transition dipole moments d_i [cf. Eq. (4)]. Optimization of the functionals J_T^{ss} or J_T^{sm} requires repeated forward and backward propagations of the initial and target states.

III. EXCITED-STATE WAVE PACKET REPRESENTING INITIAL STATE FOR STABILIZATION

The initial wave packet for the stabilization step is created by the photoassociation pulse. The simplest pulse that can be employed for the three-photon photoassociation is a transform-limited (TL) Gaussian pulse. The intensity of the laser pulse is chosen to be in the perturbative weak-field regime, where the composition of the photoassociated wave packet reflects the bandwidth of the laser pulse combined with the vibrationally averaged three-photon electric dipole transition moments between the initial scattering state and the excited-state vibrational levels below ${}^2S(5s) + {}^2P_{1/2}(6p)$ dissociation limit. A pulse duration of 4 ps full width at half maximum (FWHM) is considered, corresponding to a spectral bandwidth of 3.7 cm^{-1} . The pulse is red detuned by 12 cm^{-1} from the ${}^2S(5s) \rightarrow {}^2P_{1/2}(6p)$ atomic three-photon transition. In order to utilize broadband femtosecond laser pulses, more elaborate pulse shapes will be required that suppress the excitation of atoms [22] while possibly maximizing free-to-bound transitions. However, the general features of the photoassociated wave packet are determined by the three-photon matrix elements. They are the largest close to the ${}^2S(5s) + {}^2P_{1/2}(6p)$ dissociation limit, corresponding to a photoassociation window at interatomic separations between

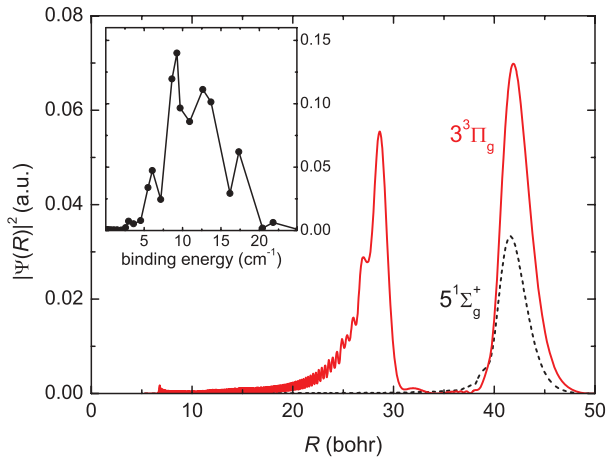


FIG. 4. (Color online) Wave packet obtained after photoassociation with a transform-limited pulse. The pulse duration is 4 ps (FWHM) and a snapshot 2.5 ps after the photoassociation pulse maximum is shown. At this time, the $(6) ^1\Sigma_g^+$ component is insignificant and not visible on the scale of this figure. Inset shows the decomposition of the wave packet onto the vibrational levels of the coupled $(5) ^1\Sigma_g^+$, $(6) ^1\Sigma_g^+$, and $(3) ^3\Pi_g$ states.

$30a_0$ and $50a_0$. Transition moments to the vibrational levels detuned by more than 30 cm^{-1} from the $^2S(5s) + ^2P_{1/2}(6p)$ threshold, corresponding to photoassociation windows at shorter interatomic separations, are significantly smaller. The most important contributions to the photoassociated wave packet will therefore remain the same as in our simple example. It could turn out that, using coherent control, photoassociation into wave packets with binding energies larger than 30 cm^{-1} becomes feasible. In this case, the stabilization of the photoassociated molecules becomes easier, and their faster vibrational dynamics and larger Franck-Condon factors to the deeply bound $X^1\Sigma_g^+$ vibrational levels will only improve the predictions of the present study. The initial wave packet for the stabilization step is plotted in Fig. 4. The inset shows the decomposition of the wave packet onto the vibrational levels of the coupled $(5) ^1\Sigma_g^+$, $(6) ^1\Sigma_g^+$, and $(3) ^3\Pi_g$ states. The binding energy of the wave packet amounts to 11.55 cm^{-1} . The snapshot shown in Fig. 4 is taken 2.5 ps after the maximum of the photoassociation pulse (i.e., before the pulse is over). At this time, the Gaussian character of the wave packet is still apparent, while at later times the strongly anharmonic shape of the potential-energy curves leads to strong wave-packet dispersion. Note that the photoassociated wave packet shows a truly mixed character with about 65% of its norm residing on the $(3) ^3\Pi_g$ triplet component and 35% on the $(5) ^1\Sigma_g^+$ singlet component. This is despite the fact that electric dipole transitions are allowed only between the atomic pair in the $a^3\Sigma_u^+$ lowest triplet state and the $(3) ^3\Pi_g$ triplet component of the coupled electronically excited manifold dissociating into $^2S(5s) + ^2P_{1/2}(6p)$ and illustrates the strong spin-orbit coupling. The role of the spin-orbit coupling is further evidenced by the double-peak structure of the wave packet with the short-range peak corresponding to the outer turning point of the $(3) ^3\Pi_g$ potential and the long-range peak reflecting the outer turning point of the $(5) ^1\Sigma_g^+$ potential. The importance of the strong resonant spin-orbit coupling for the stabilization

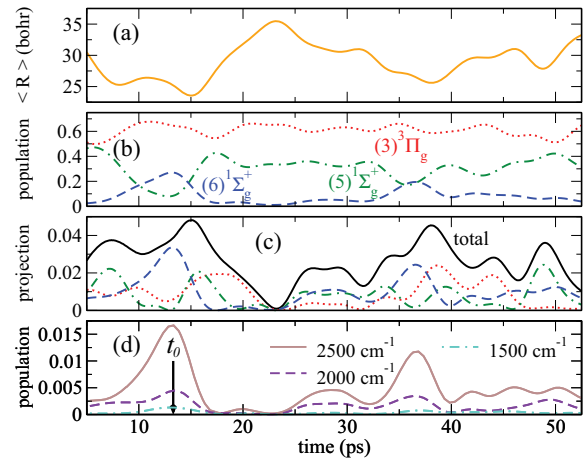


FIG. 5. (Color online) (a) Time evolution of the average bond length of the wave packet. (b) Time evolution of the populations of the $(5) ^1\Sigma_g^+$, $(6) ^1\Sigma_g^+$, and $(3) ^3\Pi_g$ components of the wave packet. (c) Projection of the time-dependent wave packet and its $(5) ^1\Sigma_g^+$, $(6) ^1\Sigma_g^+$, and $(3) ^3\Pi_g$ components onto all vibrational levels of the $X^1\Sigma_g^+$ ground electronic states with binding energies up to 1000 cm^{-1} . (d) Population of the $X^1\Sigma_g^+$ component of the wave function after stabilization with a TL pulse vs time delay between photoassociation and stabilization pulse for three different detunings, taken with the respect to the $^2P_{1/2}(6p) \rightarrow ^2S(5s)$ two-photon transition. The stabilization pulse has a FWHM of 100 fs and an integrated pulse energy of 25.4 nJ corresponding to the weak-field regime. The arrow indicates $t_0 = 13.3 \text{ ps}$ chosen as the time delay between the photoassociation and stabilization pulse peaks.

of photoassociated molecules has been discussed extensively [29–34,58]. In the present study, we will not only use it for improved transition matrix elements to deeply bound ground-state levels, but also to convert an atom pair colliding in the triplet state to singlet molecules [35]. The initial wave packet propagates toward shorter interatomic separations under the influence of the excited-state potentials. At large interatomic separations, the potential-energy curve of the $(5) ^1\Sigma_g^+$ state displays a strong $-1/R$ ion-pair character. The singlet-triplet oscillations are analyzed in Fig. 5(a) displaying the singlet and triplet components of the wave packet evolving after the photoassociation pulse in the manifold of electronically excited states. The population of the $(3) ^3\Pi_g$ triplet component oscillates around 60%, whereas the population of the $(6) ^1\Sigma_g^+$ component, that was absent just after photoassociation, reaches a maximum of 27% at $t = 12.7 \text{ ps}$ after the peak of the photoassociating pulse. A second maximum of the $(6) ^1\Sigma_g^+$ component is observed after a period of 20.1 ps and a third one after another 36.2 ps. The times at which the $(6) ^1\Sigma_g^+$ component reaches maximal values can be interpreted as moments when the wave packet arrives at its shortest distance and is reflected from the innermost repulsive short-range wall. This observation is confirmed by calculating the average bond length of the wave packet, shown in Fig. 5(b), which allows us to estimate the revival time of the present wave packet to be between 20 and 30 ps. This estimate agrees with the range of revival times, defined by $T_{\text{rev}}(v) = 2h/|E_{v+1} + E_{v-1} - 2E_v|$ [59], for the vibrational levels v that make up a wave packet with binding energies close to 12 cm^{-1} .

The knowledge of the revival time of the wave packet is useful for the interpretation of the projections of the time-dependent wave packet, $|\langle \Psi_{\text{in}}(t) | v'' \rangle|^2$, onto the vibrational levels v'' of the $X^1\Sigma_g^+$ ground electronic state, shown in Fig. 5(c) for all ground-state levels with binding energies up to 1000 cm^{-1} . These projections are largest when the wave packet is localized at its inner turning point [cf. Fig. 5(b)]. The time at which the projections show maxima correspond to optimal time delays between photoassociation and stabilization pulse. The times in between these maxima are given by the revival time. However, the transition probability does not only depend on the overlap of initial and final wave function, but also on the dipole moments and the topology of the intermediate state surfaces and their coupling. This is illustrated by the difference between Figs. 5(c) and 5(d) with Fig. 5(b) showing the calculated population on the $X^1\Sigma_g^+$ ground electronic state as a function of the time delay between photoassociation and stabilization pulse for three different detunings of the stabilization pulse. The $X^1\Sigma_g^+$ population is obtained by solving the time-dependent Schrödinger equation for a weak TL stabilization pulse. The positions of the maxima and minima of the final $X^1\Sigma_g^+$ state population correspond to those of the projection of the $(6)^1\Sigma_g^+$ component [dashed blue line in Fig. 5(c)] rather than the total projection [black line in Fig. 5(c)]. This suggests that the transition from the $(6)^1\Sigma_g^+$ component is the most important one in the stabilization process.

Based on the time-dependence of the projection and the stabilization probability analyzed in Fig. 5, we choose $t_0 = 13.3 \text{ ps}$ for the time delay, taken between the peak of the photoassociating pulse and the center of all pulses used in the following sections.

IV. STABILIZATION TO ELECTRONIC GROUND STATE WITH TRANSFORM-LIMITED AND LINEARLY CHIRPED PULSES

We first study transform-limited and linearly chirped stabilization pulses in order to understand the role of the basic pulse parameters such as intensity and spectral width and to investigate dynamical effects. By comparing projections and actual final-state populations in the previous section, we have shown that a simple two-photon Franck-Condon principle does not correctly capture the stabilization dynamics. A less simplified picture is obtained by taking the structure of the vibrational levels in the initial, intermediate, and final electronic states fully into account, neglecting strong-field effects and a dynamical interplay between pulse and spin-orbit couplings. Specifically, in the weak-field regime and for TL pulses, the probability of the resonant two-photon transition is obtained by perturbation theory. It is determined by the effective two-photon transition moment,

$$D(v'') = \sum_{v'} \left| \sum_{j=2,3,4} \langle \Psi_{\text{in}} | d_j | v' \rangle \langle v' | d_1 | v'' \rangle \right| e^{\Delta\omega_{v'}^2 / 2\sigma_\omega^2}, \quad (12)$$

where $\langle \Psi_{\text{in}} | d_j | v' \rangle = \sum_{i,i'} \int \Psi_{\text{in}}^i(R)^* d_j(R) \chi_{v'}^{i'}(R) dR$ denotes the electric transition dipole moment between the initial wave packet with components i in the $(5)^1\Sigma_g^+$, $(6)^1\Sigma_g^+$, and $(3)^3\Pi_g$

manifold and the intermediate vibrational levels v' with components i' in the excited $A^1\Sigma_u^+$ and $b^3\Pi_g$. Correspondingly, $\langle v' | d_1 | v'' \rangle$ is the electric transition dipole moment between the intermediate levels v' of the $A^1\Sigma_u^+$ and $b^3\Pi_g$ states and the final ground $X^1\Sigma_g^+$ state vibrational level v'' . The exponent accounts for the bandwidth of the laser pulse, σ_ω , and the detuning of the intermediate levels from the laser frequency,

$$\Delta\omega_{v'} = \omega_{2P_{1/2}(5p)} - \omega_{v'} + \omega_{v''} - \omega_L. \quad (13)$$

The laser frequency ω_L is chosen such that the two-photon transition is resonant for the initial wave packet and the final level v'' , $\omega_L = (\omega_{2P_{1/2}(6p)} - \omega_{\text{in}} + \omega_{v''})/2$. Here, ω_{in} denotes the binding energy of the initial wave packet, defined to be positive, and $\omega_{2P_{1/2}(np)}$ is the excitation energy of the $2P_{1/2}(np)$ atomic level. The spectral width is given in terms of the FWHM of the time profile of the pulse τ , $\sigma_\omega = 2\sqrt{2 \ln(2)}/\tau$. The two-photon transition moments, defined by Eq. (12), are shown in Fig. 6 for all vibrational levels v'' of the $X^1\Sigma_g^+$ ground electronic state. The large peak around a binding energy of 2650 cm^{-1} indicates that stabilization of the excited-state wave packet to levels with binding energies in this range is most efficient. The peak maximum in Fig. 6 corresponds to a transition to the vibrational level $v'' = 23$, with a binding energy $E_{v''} = 2651 \text{ cm}^{-1}$. This suggests that the level $v'' = 23$ might be a good choice for the target in the state-to-state optimization of stabilization process below in Sec. V. A standard choice of 100 fs pulse duration for the TL pulse, corresponding to a spectral width of about 150 cm^{-1} FWHM

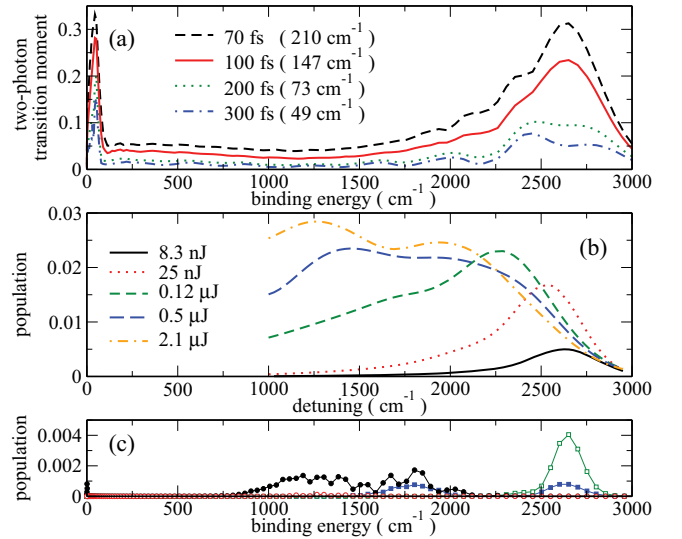


FIG. 6. (Color online) (a) Resonant two-photon transition moments defined by Eq. (12) vs binding energy of the target $X^1\Sigma_g^+$ state levels v'' for four different pulse durations or spectral widths, respectively. (b) Final population of the $X^1\Sigma_g^+$ state after a TL 100 fs pulse vs pulse detuning, taken with the respect to the $2P_{1/2}(6p) \rightarrow 2S(5s)$ atomic two-photon transition, for five different integrated pulse energies. (c) Vibrational decomposition of the $X^1\Sigma_g^+$ component of the wave function after stabilization with TL 100 fs pulses with different pulse energies and detunings with the respect to $2P_{1/2}(6p) \rightarrow 2S(5s)$ atomic two-photon transition: \square 25.4 nJ and 2650 cm^{-1} , \blacksquare $2.06 \mu\text{J}$ and 2650 cm^{-1} , \circ 25.4 nJ and 1240 cm^{-1} , \bullet $2.06 \mu\text{J}$ and 1240 cm^{-1} .

is sufficient to address a broad distribution of target vibrational levels in the $X^1\Sigma_g^+$ state.

The integrated pulse energy is given by

$$E = \varepsilon_0 c A \int_0^\infty |\epsilon(t)|^2 dt, \quad (14)$$

with $\epsilon(t)$ being the laser field, $A = \pi r^2$ being the area which is covered by the laser ($r = 50 \mu\text{m}$ was assumed), c being the speed of light, and ε_0 being the dielectric constant. We use the integrated pulse energy rather than the peak intensity of the pulse since, independently of the pulse duration, it quantifies the energy pumped into the molecule.

The two-photon transition probability can be predicted from the effective two-photon transition moment [cf. Eq. (12) and Fig. 6] only in the weak-field regime when dynamic Stark shifts and other time-dependent effects do not play any role. The dependence of the two-photon transition probability on the pulse intensity and detuning,

$$\Delta\omega_L = 2\omega_L - \omega_{P_{1/2}(6p)}, \quad (15)$$

is illustrated in Fig. 6(b). The pulse duration is kept fixed at 100 fs FWHM. For weak and intermediate pulse intensities, with the integrated pulse energy corresponding to 8.3 and 25.4 nJ, the final $X^1\Sigma_g^+$ ground-state population as a function of the pulse detuning reflects the shape of the effective two-photon transition moment [Fig. 6(a)]. On the other hand, the final $X^1\Sigma_g^+$ population decreases for the detuning corresponding to the maximum of the two-photon transition moment and increases for smaller detunings when the integrated pulse energy is increased. This observation is rationalized in terms of the strong dynamic Stark shift by analyzing the vibrational distribution of the final $X^1\Sigma_g^+$ state population in Fig. 6(c) for a detuning $\Delta\omega_L = 2650 \text{ cm}^{-1}$, corresponding to the maximum of the two-photon transition moment in Fig. 6(a). When increasing the integrated pulse energy from 25.4 nJ to 2 μJ (i.e., from the intermediate- to the strong-field regime), two peaks are observed in the vibrational distribution rather than a single Gaussian around the binding energy of $v'' = 23$, reflecting the bandwidth of the pulse. In the strong-field regime, one peak of the vibrational distribution is still located around the binding energy of the resonant level, while the second one is shifted by 800 cm^{-1} to smaller binding energies. This is due to the positive differential Stark shift caused by the coupling to the intermediate states, which indeed increases the energy separation between ground and excited states by about 800 cm^{-1} . The dynamic Stark shift of the ground-state vibrational level v'' is estimated according to

$$\omega_S^{v''} = -\frac{1}{2} |\epsilon(t)|^2 \sum_{v'} |\langle v'' | \hat{\mathbf{d}}_e | v' \rangle|^2 \frac{\omega_{v'v''}}{\omega_{v'v''}^2 - \omega_L^2}, \quad (16)$$

where $\langle v'' | \hat{\mathbf{d}}_e | v' \rangle$ is the electric transition dipole moment, $\omega_{v'v''}$ is the transition frequency between levels v' and v'' , and ω_L denotes the laser frequency. Figure 6(c) compares the final-state vibrational distribution for two different detunings of the stabilization pulse, $\Delta\omega_L = 2650 \text{ cm}^{-1}$ corresponding to the peak of the two-photon transition probability for weak

and intermediate fields [black dotted and red solid curves in Fig. 6(b)] and $\Delta\omega_L = 1240 \text{ cm}^{-1}$ corresponding to the peak of the two-photon transition probability for strong fields [black dot-dashed curve in Fig. 6(b)]. Inspection of the vibrational distributions in Fig. 6(c) reveals that, for $\Delta\omega_L = 1240 \text{ cm}^{-1}$ and 2 μJ integrated pulse energy, a peak at binding energies larger than the detuning appears. Also, this peak is caused by the differential Stark shift which this time is negative, decreasing the energy separation between ground and excited states by about 600 cm^{-1} . In the weak- and intermediate-field regimes, almost no population is transferred for $\Delta\omega_L = 1240 \text{ cm}^{-1}$ [red empty circles in Fig. 6(c)], confirming a strong-field effect.

The total population that is transferred by a TL pulse, with 100 fs FWHM and a detuning in the range of 2500 to 2600 cm^{-1} , from the initial wave packet to the $X^1\Sigma_g^+$ ground electronic state amounts to up to 1.7% in the weak- and intermediate-field regimes. For strong fields, up to 2.9% of the population can be transferred for detunings between 1000 and 1500 cm^{-1} and pulse energies above 1 μJ . The subsequent analysis is restricted to pulses with detunings between 2500 and 2650 cm^{-1} , corresponding to the maximum of the effective two-photon transition moment where the smallest pulse intensities should be required. As apparent from Fig. 6, the dynamic Stark shift is detrimental to efficient population transfer by the stabilization pulse. One option to increase the integrated pulse power while keeping the maximum field intensity and thus the dynamic Stark shift small is to consider a train of short TL pulses. A second option is given by chirping the pulse. The efficiency of the two-photon population transfer to the electronic ground with the first option, a train of 100 fs TL pulses delayed relative to each other by 200 fs and with a sinusoidal envelope, is analyzed in Fig. 7. While increasing the pulse energy of a 100 fs pulse does not improve the population transfer to the electronic ground state beyond 1.7%, a train of pulses yields up to about 6% for pulse energies that are still in the nJ range. The population transfer with a train of short pulses can be interpreted as the cumulative result of many single transitions that accumulate amplitude in the $X^1\Sigma_g^+$ ground state. Using a train of pulses instead of a single pulse with the same bandwidth, one can produce 3.5 times more ground-state molecules. Figure 7 thus confirms that the Stark shift is responsible for the comparatively inefficient population transfer observed for TL pulses. From the coherent control of atomic transitions using strong fields, it is known that the influence of the dynamic Stark shift can be compensated by chirping the pulse [14,15]. We investigate in Fig. 8(a), which shows the final ground-state population vs chirp rate for increasing pulse energy, whether this approach works also for molecular transitions. We use a positive chirp to correct the influence of the dynamic Stark shift since the differential Stark shift for stabilization to vibrational levels with binding energies close to 2650 cm^{-1} is positive. Chirping a weak-field pulse (black dot-dashed curve) deteriorates the population transfer. When more energetic pulses are used, chirping increases the final $X^1\Sigma_g^+$ state population from 1.5% for unchirped pulses to almost 9% for the best-chirped pulses. In total we find that chirping the pulse improves the stabilization process and enhances the amount of ground-state population by a factor of about six. Figure 8(b) showing the final-state

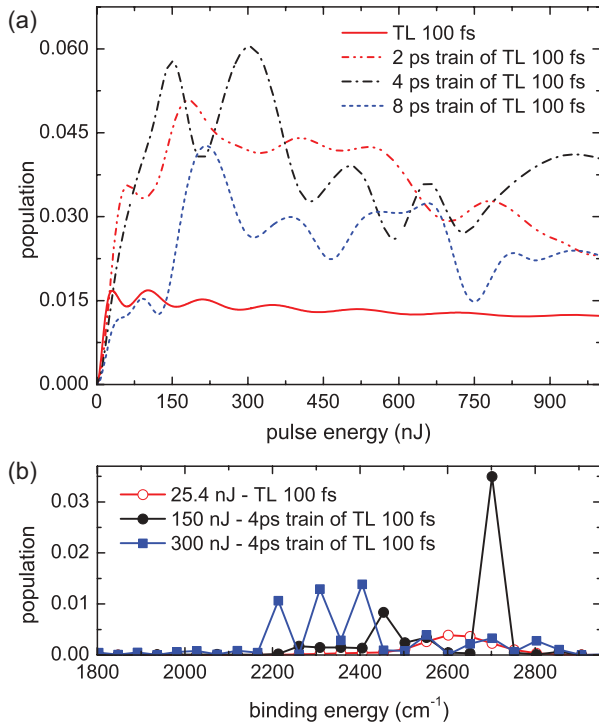


FIG. 7. (Color online) (a) $X^1\Sigma_g^+$ state population after a 100 fs TL pulse (solid line) and a train of 100 fs TL pulses (dashed and dotted lines) vs integrated pulse energy. (b) $X^1\Sigma_g^+$ state vibrational distribution after stabilization with a 100 fs TL pulse and 4 ps train of 100 fs TL pulses. The pulse detuning is 2500 cm^{-1} taken with the respect to the ${}^2P_{1/2}(6p) \rightarrow {}^2S(5s)$ atomic two-photon transition.

vibrational distribution confirms that the same mechanism as in the atomic case is at work [14,15]: When increasing the pulse energy from 25.4 to 300 nJ without chirping the pulse, a second peak shifted by 500 cm^{-1} appears. The energies of the levels of this second peak correspond exactly to the detuning corrected by the Stark shift. A linear chirp introduces a time-dependent instantaneous frequency of the pulse, $\omega(t) = \omega_L + \chi t/2$, with χ being the temporal chirp rate. When chosen correctly, the chirp compensates the phase that the molecules accumulate due the Stark shift and thus prevents the transition to shift out of resonance. This leads to the strong enhancement of the stabilization efficiency observed in Fig. 8.

Our investigation of the stabilization dynamics under TL and linearly chirped pulses shows that simply replacing a strong TL pulse by a train of pulses with the same total integrated pulse energy or linearly chirping the pulse can enhance the stabilization probability from 1% up to 9%. The reason for the enhancement is given by the weaker Stark shifts for smaller peak intensities and compensation of the phase accumulated due to the Stark shift by a linear chirp. In the following section we employ optimal control theory to calculate the optimum detunings and pulses shapes. This allows us to determine the maximum number of ground-state molecules that can be produced for a given integrated pulse energy.

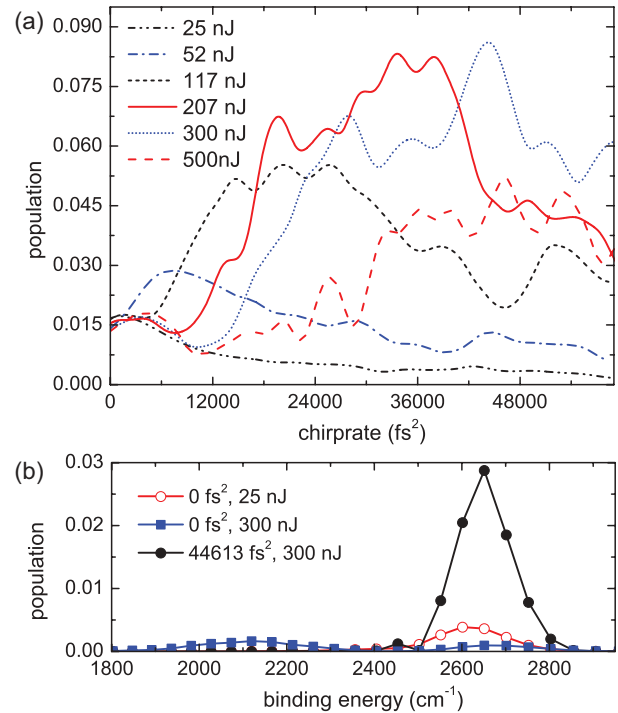


FIG. 8. (Color online) (a) Final $X^1\Sigma_g^+$ state population after linearly chirped pulses with a TL FWHM of 100 fs vs chirp rate for different pulse energies. (b) $X^1\Sigma_g^+$ state vibrational distribution after stabilization with a weak TL pulse, a TL pulse, and a chirped strong pulse. The pulse detuning is 2500 cm^{-1} taken with the respect to the ${}^2P_{1/2}(6p) \rightarrow {}^2S(5s)$ atomic two-photon transition.

V. STABILIZATION TO ELECTRONIC GROUND STATE WITH OPTIMALLY SHAPED PULSES

We employ the optimization algorithm described in Sec. II C to find those laser pulses that stabilize the initial wave packet most efficiently to the $X^1\Sigma_g^+$ electronic state. The final $X^1\Sigma_g^+$ state population, shown in Fig. 9(a), converges smoothly to the maximal value that can be obtained with a given pulse duration, displayed in Fig. 9(b). The maximum stabilization probability for a pulse duration of 1 ps is 14%. Increasing the pulse duration, the stabilization probability reaches 26% for 2 ps pulses and 67% for 10 ps pulses. The integrated pulse energies of the optimized pulses vary between 80 and 150 nJ. This is two to three times smaller than the integrated pulse energies for the trains of pulses and the linearly chirped pulses discussed in Sec. IV. The guess pulse for the optimizations shown in Fig. 9 is a TL pulse with a pulse duration of 100 fs and integrated pulse energy of 10 nJ. For all the results presented here, the state-to-manifold-of-states functional, Eq. (9), was employed. The results obtained by using the state-to-state functional, Eq. (8), do not differ significantly. In particular, the same bounds on the maximum stabilization efficiencies are observed. However, for the state-to-state functional, the optimizations were found to converge slower. This is easily rationalized in terms of a single state being a more restrictive optimization target than a manifold. The integrated energy of the optimal pulses presented in Fig. 9(b) does not depend strongly on the

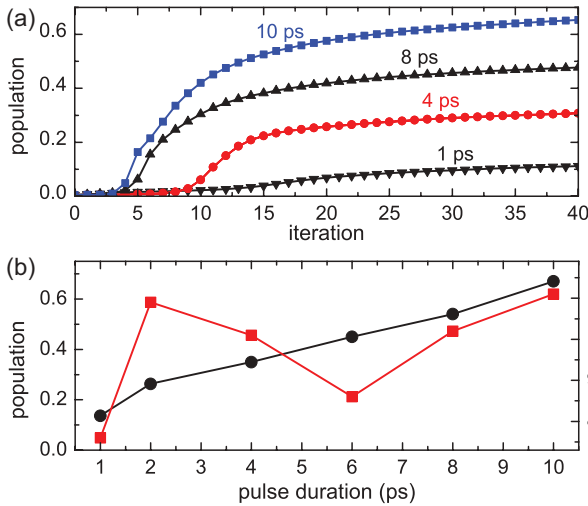


FIG. 9. (Color online) (a) Final $X^1\Sigma_g^+$ state population after optimized pulses of different pulse duration vs number of iteration steps. (b) Final $X^1\Sigma_g^+$ state population (left scale, black circles) and corresponding pulse energy (right scale, red squares) vs pulse duration. The values were collected after 50 iterations, starting with the same weak-field guess pulse ($E = 10$ nJ) and using the same weight, $\lambda = 400$ in all optimizations.

optimal pulse duration. The slightly oscillatory behavior of the integrated pulse energy as a function of pulse duration is observed irrespective of the shape and energy of the guess pulse and the weight λ .

The fact that the maximum population transfer to the $X^1\Sigma_g^+$ state is clearly less than 100% is due to the pulses being too short to drive the complete wave packet to the ground state [60]. When the pulse duration is much shorter than the time scale of the vibrational motion and spin-orbit oscillations, then only that part of the wave packet that shows a favorable overlap with the target state during the optimization window is transferred. For example, the pulse with 1 ps duration essentially reflects the overlap of the initial wave packet. By increasing the pulse duration [cf. Fig. 9(b)], the stabilization efficiency increases monotonically. A stabilization probability of 100% is expected once the pulse duration is longer than the revival time of the wave packet, estimated above to be between 20 and 30 ps. In fact, optimizations with pulse durations of 20 and 30 ps yield stabilization efficiencies of 93% and 99%, respectively, with pulse energies below 150 nJ. However, we restrict our analysis to pulse durations up to 10 ps since stretching a TL 100 fs pulse by more than a factor of 100 due to pulse shaping is not realistic. Analyzing the time evolution of the population on each of the electronic states during an optimized pulse of 10 ps pulse duration, the molecules are found to first accumulate in the intermediate $^1\Sigma_u^+$ and $b^3\Pi_u$ states before being dumped to the $X^1\Sigma_g^+$ electronic ground state. The example of an optimized pulse with pulse duration of 8 ps is presented in Fig. 10. Inspection of the optimized pulse during a short interval of 400 fs [Fig. 10(b)], reveals that each peak of the pulse amplitude is correlated to a change of the temporal phase by π . The spectrum, Fig. 10(c), displays two pronounced peaks with maxima at ± 400 cm^{-1} with respect to the central

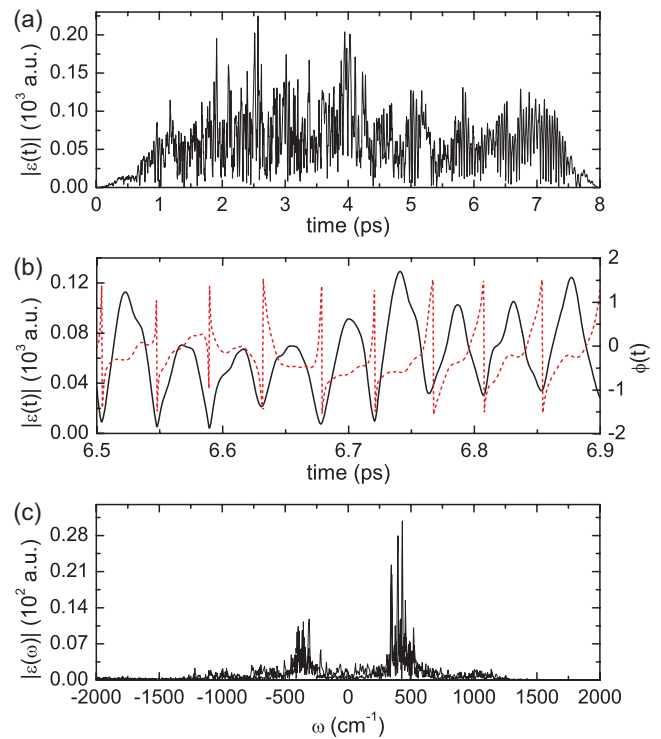


FIG. 10. (Color online) Temporal envelope (a) and spectrum (c) of an optimized pulse. (b) Envelope (left scale, solid black line) and temporal phase (right scale, red dashed line) of the optimized pulse in a short time interval.

laser frequency. The disappearance of the central frequency during the optimization and appearance of two slightly detuned frequencies is somewhat surprising since the central frequency was chosen to maximize the effective two-photon transition moment. There are two possibilities to rationalize this result of the optimization: Either the detuning shifted by the additional 400 cm^{-1} is better and should be chosen for the guess pulse, or the absorption of two photons with different energies is more optimal than that of two identical photons. The latter explains the observed optimal spectrum: Analysis of the electric transition dipole moment between the initial wave packet and the intermediate vibrational levels, $\langle \Psi_{\text{in}} | \hat{\mathbf{d}}_e | v' \rangle$, reveals that it takes its maximal value for levels v' that are detuned from the frequency corresponding to the maximum of the effective two-photon transition moment, Eq. (12), by 460 cm^{-1} . The electric transition dipole moment between the intermediate and ground-state vibrational level, $\langle v' | \hat{\mathbf{d}}_e | v'' \rangle$, attains its maximum for a transition frequency that is smaller than the laser frequency corresponding to the maximum of the effective two-photon transition moment by 250 cm^{-1} . Note that the transition moments for absorption of the first photon, $\langle \Psi_{\text{in}} | \hat{\mathbf{d}}_e | v' \rangle$, are about 7 times smaller than those for absorption of the second photon, $\langle v' | \hat{\mathbf{d}}_e | v'' \rangle$. The effective two-photon transition moment is obtained as a compromise of the two one-photon transition moments [cf. Eq. (12)]. Allowing for two photons of different energy in the calculation of the effective two-photon transition moment, we still find a peak for a ground-state binding energy of 2650 cm^{-1} , which is at best 40% higher when energies of photons are detuned by ± 390 cm^{-1} . It corresponds to the transition frequency from

the initial wave packet to the intermediate state being 390 cm^{-1} larger and that between the intermediate state and the ground electronic state being 390 cm^{-1} smaller than the frequency for a transition with two identical photons. Equipped with this information, we can construct a guess pulse that is the sum of two TL pulses with their central frequencies separated by 780 cm^{-1} . In this case, half of the integrated guess pulse energy is sufficient to reach the same initial stabilization probability, reflecting the stronger effective two-photon transition moment. Optimization with such a guess pulse converges faster and the final integrated pulse energy of the optimized pulse is smaller (data not shown) but the bound for the stabilization efficiency, Fig. 9, remains in place. The spectrum of the optimized pulse with two peaks separated by 780 cm^{-1} is very similar to the one shown in Fig. 10, irrespective of the guess pulse central frequency. In particular, the width of each of the peaks roughly corresponds to the bandwidth of a TL 100 fs pulse.

Optimization of the stabilization pulse reveals that the upper bound of the stabilization efficiency, found to be 9% for linearly chirped pulses, can be increased up to 67% when a TL pulse of 100 fs pulse duration is shaped and stretched to 10 ps. This is significantly more efficient than any existing proposal for short-pulse photoassociation [5,61,62]. At the same time, the integrated pulse energies of the optimized pulses are below 150 nJ, two to three times less than those found for the best linearly chirped pulses or trains of TL pulses in Sec. IV. The shape of the optimized pulse is comparatively simple, characterized by a sequence of short pulses with linear and quadratic chirps.

VI. SUMMARY AND CONCLUSIONS

Based on state-of-the-art *ab initio* calculations, we have studied the optical production of Rb_2 molecules in their electronic ground state using multiphoton transitions that are driven by short laser pulses. Our model includes not only accurate potential-energy surfaces but also spin-orbit couplings, Stark shifts, and transition matrix elements. We have employed a nonperturbative treatment of the light-matter interaction which is crucial to capture the strong-field effects that often accompany multiphoton transitions.

Our proposal for the optical production of molecules using shaped femtosecond laser pulses that drive multiphoton transitions consists, in its first step, of nonresonant three-photon photoassociation of atom pairs colliding in their triplet state. A three-photon transition allows access of electronic states that vary as $1/R^3$ at long range, providing comparatively large free-to-bound transition matrix elements [22]. Strong spin-orbit interaction allows for triplet-to-singlet conversion. The stabilization pulse, time delayed with respect to the photoassociation pulse, transfers the photoassociated wave packet to the electronic ground state in a resonant two-photon transition proceeding via the $A^1\Sigma_u^+ b^3\Pi_u$ manifold. It benefits from the intricate excited-state wave packet dynamics resulting from coupled vibrational dynamics in states with partially ion-pair character and singlet-triplet oscillations due to the spin-orbit interaction.

We have studied the transfer of the excited-state wave packet to the electronic ground state using transform-limited,

linearly chirped and optimally shaped laser pulses. Linearly chirped pulses were found to perform much better, by almost an order of magnitude, than transform-limited pulses. This is due to large Stark shifts which drive the transition off resonance for transform-limited pulses. We have confirmed that a strong-field control scheme known for atomic transitions, with a linear chirp compensating the phase accumulated due to the Stark shift [14,15], can also be successfully employed for molecular transitions. In this case, the chirp rate cannot be calculated analytically but needs to be determined numerically.

Surprisingly, for optimally shaped laser pulses, the integrated pulse energy was found to be significantly lower than that of the best transform-limited and linearly chirped pulses, while yielding a much better stabilization efficiency. This is due to the fact that the transform-limited and linearly chirped laser pulses were chosen based on an effective two-photon transition matrix element assuming equal transition frequencies of both photons. Optimization reveals that a two-photon transition with two slightly different transition frequencies allows us to employ two one-photon transitions with significantly larger transition matrix elements.

Overall, the stabilization efficiency is limited by somewhat less than 70% for transform-limited 100 fs laser pulses that are stretched to 10 ps. More than 90% transfer efficiency becomes possible by stretching the pulse to 20 ps. The target level in the electronic ground state that is reached by these stabilization pulses is located more than half way down the ground-state potential well, with a binding energy of about 2600 cm^{-1} . The stabilization efficiencies reported here have to be compared to 20%, respectively 50%, for stabilization with chirped pulses in the presence of strong spin-orbit interaction to very weakly bound levels [5,61] and to a few percent for stabilization to the vibrational ground state using engineered excited-state dynamics [62]. In contrast to these earlier studies, with the current scheme it becomes possible to convert almost all of the weakly bound photoassociated molecules into truly bound ground-state molecules from where a single subsequent Raman step is sufficient to transfer these molecules into their vibronic ground state. Such a significant improvement for comparatively short stabilization pulses is afforded by a speedup of the dynamics due to the partial ion-pair character of the excited-state potential curves and population trapping at short interatomic separations due to the strong spin-orbit interaction. It emphasizes the usefulness of multiphoton transitions, which allow us to access these electronic states, for the photoassociation of ultracold atoms.

Multiphoton transitions, moreover, allow the utilization of the full bandwidth of a femtosecond pulse for photoassociation and stabilization. They also provide more flexibility with respect to the transition frequencies that can be addressed. The basic features of femtosecond laser pulses—their broad bandwidth and pulse shaping capabilities—can then be used to full advantage. Our results thus pave the way toward the coherent control of photoassociation at very low temperature. They are not restricted to rubidium but rather are applicable to any molecule that shows the main features of the dynamics studied here—an ion-pair potential that is coupled to covalent states and strong spin-orbit interaction.

Future work will consider optimization of the photoassociation pulse. This represents a nontrivial control problem since the initial state of photoassociation is the thermally populated continuum of scattering states. While a thermal ensemble is inherently incoherent, quantum effects are already perceptible due to the low temperature. It will be interesting to see whether an optimally shaped pulse can make use of the enhanced quantum purity and the presence of correlations at low temperature.

ACKNOWLEDGMENTS

We would like to thank Ronnie Kosloff for many fruitful discussions. Financial support from the Polish Ministry of Science and Higher Education through the project N N204 215539 is gratefully acknowledged. M.T. is supported by the project operated within the Foundation for Polish Science MPD Programme cofinanced by the EU European Regional Development Fund.

-
- [1] K. M. Jones, E. Tiesinga, P. D. Lett, and P. S. Julienne, *Rev. Mod. Phys.* **78**, 483 (2006).
- [2] S. A. Rice and M. Zhao, *Optical Control of Molecular Dynamics* (John Wiley and Sons, New York, 2000).
- [3] P. Brumer and M. Shapiro, *Principles and Applications of the Quantum Control of Molecular Processes* (Wiley Interscience, Hoboken, New Jersey, 2003).
- [4] C. P. Koch and M. Shapiro, *Chem. Rev.* **212**, 4928 (2012).
- [5] C. P. Koch, R. Kosloff, and F. Masnou-Seeuws, *Phys. Rev. A* **73**, 043409 (2006).
- [6] W. Salzmann, U. Poschinger, R. Wester, M. Weidemüller, A. Merli, S. M. Weber, F. Sauer, M. Plewicki, F. Weise, A. Mirabal Esparza *et al.*, *Phys. Rev. A* **73**, 023414 (2006).
- [7] B. L. Brown, A. J. Dicks, and I. A. Walmsley, *Phys. Rev. Lett.* **96**, 173002 (2006).
- [8] W. Salzmann, T. Mullins, J. Eng, M. Albert, R. Wester, M. Weidemüller, A. Merli, S. M. Weber, F. Sauer, M. Plewicki *et al.*, *Phys. Rev. Lett.* **100**, 233003 (2008).
- [9] T. Mullins, W. Salzmann, S. Götz, M. Albert, J. Eng, R. Wester, M. Weidemüller, F. Weise, A. Merli, S. M. Weber *et al.*, *Phys. Rev. A* **80**, 063416 (2009).
- [10] A. Merli, F. Eimer, F. Weise, A. Lindinger, W. Salzmann, T. Mullins, S. Götz, R. Wester, M. Weidemüller, R. Aġanoġlu *et al.*, *Phys. Rev. A* **80**, 063417 (2009).
- [11] D. J. McCabe, D. G. England, H. E. L. Martay, M. E. Friedman, J. Petrovic, E. Dimova, B. Chatel, and I. A. Walmsley, *Phys. Rev. A* **80**, 033404 (2009).
- [12] D. Meshulach and Y. Silberberg, *Nature (London)* **396**, 239 (1998).
- [13] D. Meshulach and Y. Silberberg, *Phys. Rev. A* **60**, 1287 (1999).
- [14] C. Trallero-Herrero, D. Cardoza, T. C. Weinacht, and J. L. Cohen, *Phys. Rev. A* **71**, 013423 (2005).
- [15] C. Trallero-Herrero, J. L. Cohen, and T. Weinacht, *Phys. Rev. Lett.* **96**, 063603 (2006).
- [16] C. Trallero-Herrero and T. C. Weinacht, *Phys. Rev. A* **75**, 063401 (2007).
- [17] A. Gandman, L. Chuntanov, L. Rybak, and Z. Amitay, *Phys. Rev. A* **75**, 031401 (2007).
- [18] A. Gandman, L. Chuntanov, L. Rybak, and Z. Amitay, *Phys. Rev. A* **76**, 053419 (2007).
- [19] L. Chuntanov, L. Rybak, A. Gandman, and Z. Amitay, *Phys. Rev. A* **77**, 021403 (2008).
- [20] L. Chuntanov, L. Rybak, A. Gandman, and Z. Amitay, *J. Phys. B* **41**, 035504 (2008).
- [21] Z. Amitay, A. Gandman, L. Chuntanov, and L. Rybak, *Phys. Rev. Lett.* **100**, 193002 (2008).
- [22] C. P. Koch, M. Ndong, and R. Kosloff, *Faraday Discuss.* **142**, 389 (2009).
- [23] L. Rybak, S. Amaran, L. Levin, M. Tomza, R. Moszynski, R. Kosloff, C. P. Koch, and Z. Amitay, *Phys. Rev. Lett.* **107**, 273001 (2011).
- [24] L. Rybak, Z. Amitay, S. Amaran, R. Kosloff, M. Tomza, R. Moszynski, and C. P. Koch, *Faraday Discuss.* **153**, 383 (2011).
- [25] R. Kosloff, S. Rice, P. Gaspard, S. Tersigni, and D. Tannor, *Chem. Phys.* **139**, 201 (1989).
- [26] T. Ban, H. Skenderović, R. Beuc, I. K. Bronić, S. Rousseau, A. Allouche, M. Aubert-Frécon, and G. Pichler, *Chem. Phys. Lett.* **345**, 423 (2001).
- [27] T. Ban, R. Beuc, H. Skenderović, and G. Pichler, *Europhys. Lett.* **66**, 485 (2004).
- [28] C. Amiot, O. Dulieu, and J. Vergès, *Phys. Rev. Lett.* **83**, 2316 (1999).
- [29] C. M. Dion, C. Drag, O. Dulieu, B. Laburthe Tolra, F. Masnou-Seeuws, and P. Pillet, *Phys. Rev. Lett.* **86**, 2253 (2001).
- [30] H. K. Pechkis, D. Wang, Y. Huang, E. E. Eyler, P. L. Gould, W. C. Stwalley, and C. P. Koch, *Phys. Rev. A* **76**, 022504 (2007).
- [31] A. Fioretti, O. Dulieu, and C. Gabbanini, *J. Phys. B* **40**, 3283 (2007).
- [32] S. Ghosal, R. J. Doyle, C. P. Koch, and J. M. Hutson, *New J. Phys.* **11**, 055011 (2009).
- [33] B. E. Londoño, J. E. Mahecha, E. Luc-Koenig, and A. Crubellier, *Phys. Rev. A* **80**, 032511 (2009).
- [34] M. Tomza, F. Pawłowski, M. Jeziorska, C. P. Koch, and R. Moszynski, *Phys. Chem. Chem. Phys.* **13**, 18893 (2011).
- [35] J. M. Sage, S. Sainis, T. Bergeman, and D. DeMille, *Phys. Rev. Lett.* **94**, 203001 (2005).
- [36] M. Ndong and C. P. Koch, *Phys. Rev. A* **82**, 043437 (2010).
- [37] V. Kokouline, O. Dulieu, R. Kosloff, and F. Masnou-Seeuws, *J. Chem. Phys.* **110**, 9865 (1999).
- [38] K. Willner, O. Dulieu, and F. Masnou-Seeuws, *J. Chem. Phys.* **120**, 548 (2004).
- [39] S. Kallush and R. Kosloff, *Chem. Phys. Lett.* **433**, 221 (2006).
- [40] R. Kosloff, *Annu. Rev. Phys. Chem.* **45**, 145 (1994).
- [41] M. Tomza, M. Musiał, R. Gonzalez-Frerez, C. P. Koch, and R. Moszynski (unpublished).
- [42] M. Musiał, *J. Chem. Phys.* **136**, 134111 (2012).
- [43] D. I. Lyakh, M. Musiał, V. F. Lotrich, and R. J. Bartlett, *Chem. Rev.* **112**, 182 (2012).
- [44] R. J. Bartlett and M. Musiał, *Rev. Mod. Phys.* **79**, 291 (2007).

- [45] T. G. A. Heijmen, R. Moszynski, P. E. S. Wormer, and A. van der Avoird, *Mol. Phys.* **89**, 81 (1996).
- [46] A. Marte, T. Volz, J. Schuster, S. Dürr, G. Rempe, E. G. M. van Kempen, and B. J. Verhaar, *Phys. Rev. Lett.* **89**, 283202 (2002).
- [47] R. F. Gutterres, C. Amiot, A. Fioretti, G. Gabbanini, M. Mazzoni, and O. Dulieu, *Phys. Rev. A* **66**, 024502 (2002).
- [48] M. Marinescu and A. Dalgarno, *Phys. Rev. A* **52**, 311 (1995).
- [49] I. S. Lim, P. Schwerdtfeger, B. Metz, and H. Stoll, *J. Chem. Phys.* **122**, 104103 (2005).
- [50] J. F. Stanton, J. Gauss, S. A. Perera, J. D. Watts, A. Yau, M. Nooijen, N. Oliphant, P. Szalay, W. Lauderdale, S. Gwaltney *et al.*, ACES II is a program product of the Quantum Theory Project, University of Florida.
- [51] H.-J. Werner, P. J. Knowles, F. R. M. R. Lindh, M. Schütz, P. Celani, T. Korona, G. Rauhut, R. D. Amos, A. Bernhardsson, A. Berning *et al.*, MOLPRO, version 2006.1, a package of *ab initio* programs (2006), see <http://www.molpro.net>.
- [52] S. J. Park, A. W. Suh, Y. S. Lee, and G.-H. Jeung, *J. Mol. Spectrosc.* **207**, 129 (2001).
- [53] D. Edvardsson, S. Lunell, and C. M. Marian, *Mol. Phys.* **101**, 2381 (2003).
- [54] A.-R. Allouche and M. Aubert-Frecon, *J. Chem. Phys.* **136**, 114302 (2012).
- [55] J. P. Palao and R. Kosloff, *Phys. Rev. A* **68**, 062308 (2003).
- [56] S. E. Sklarz and D. J. Tannor, *Phys. Rev. A* **66**, 053619 (2002).
- [57] D. M. Reich, M. Ndong, and C. P. Koch, *J. Chem. Phys.* **136**, 104103 (2012).
- [58] W. Skomorowski, R. Moszynski, and C. P. Koch, *Phys. Rev. A* **85**, 043414 (2012).
- [59] I. S. Averbukh and N. F. Perelman, *Phys. Lett. A* **139**, 449 (1989).
- [60] C. P. Koch, J. P. Palao, R. Kosloff, and F. Masnou-Seeuws, *Phys. Rev. A* **70**, 013402 (2004).
- [61] C. P. Koch, E. Luc-Koenig, and F. Masnou-Seeuws, *Phys. Rev. A* **73**, 033408 (2006).
- [62] C. P. Koch and R. Moszyński, *Phys. Rev. A* **78**, 043417 (2008).
- [63] Specifically, the population of the (7) $^1\Sigma_g^+$ and (4) $^3\Pi_g$ states at an instant in time was smaller by a factor 100 or more than the population of the (5) $^1\Sigma_g^+$, (6) $^1\Sigma_g^+$, and (3) $^3\Pi_g$ states.